Fracture and aftershock distribution illuminate two styles of failure around faults

Alba M. Rodriguez Padilla[1], Michael E. Oskin[1], Christopher Milliner[2]

[1]University of California, Davis; [2]California Institute of Technology, Pasadena, CA.

UC DAVIS DEPARTMENT of EARTH AND PLANETARY SCIENCES

SCEC AN NSF+USGS CENTER

Poster 138

Contribution #10578

Introduction

The Ridgecrest earthquake sequence struck in July 2019 rupturing a series of orthogonal right-lateral and left-lateral faults in the best-monitored continental earthquake sequence to date. The excellent spatiotemporal coverage offers the opportunity to compare surface displacements, fractures and shallow aftershocks (<5 km) at the meter-scale to understand failure processes and stress distribution around the main surface rupture.

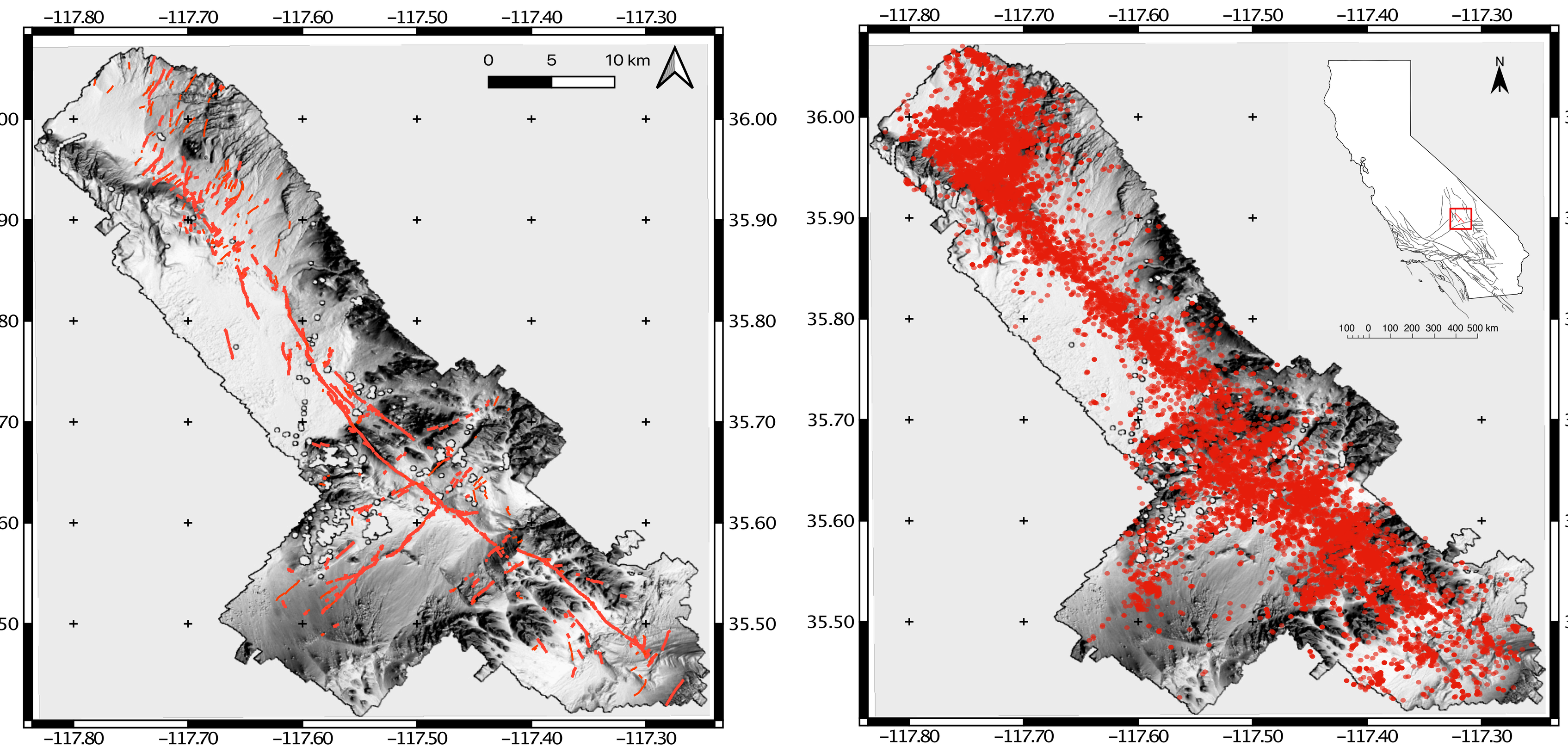

Figure 1: Left: Surface fractures mapped from the Ridgecrest lidar DEM (Hudnut et al., 2020). See poster 019. Right: Seismicity between July 4 and July 25, 2020 from the Ridgecrest QTM catalog (Ross et al., 2019).

Orientation

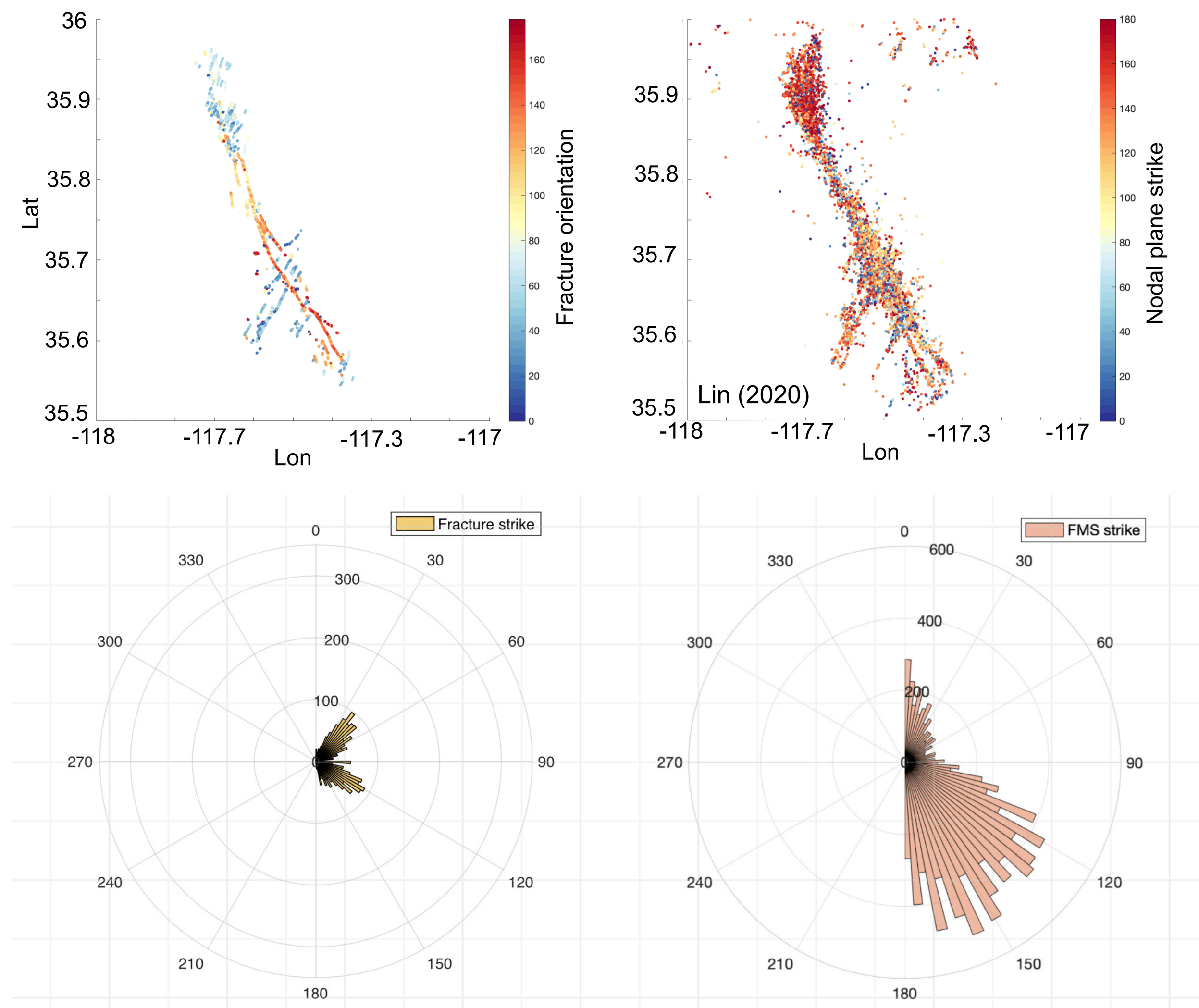

Figure 2: Top: Spatial distribution of fracture (left) and nodal plane strike (right). Bottom: Rose diagrams of fracture orientations (left) and nodal plane strike (right).

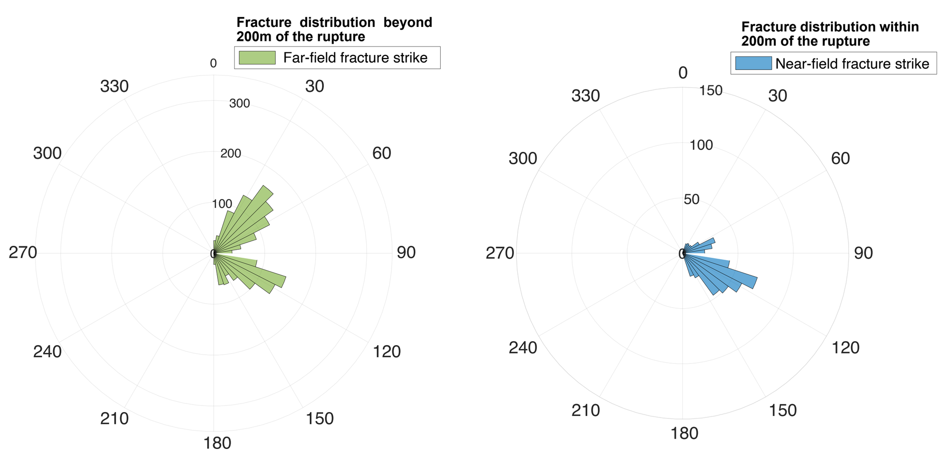

Figure 4: Near-field (<200 m from fault) and far-field (200m +) distribution of surface fractures. Both orthogonal and conjugate sets are present.

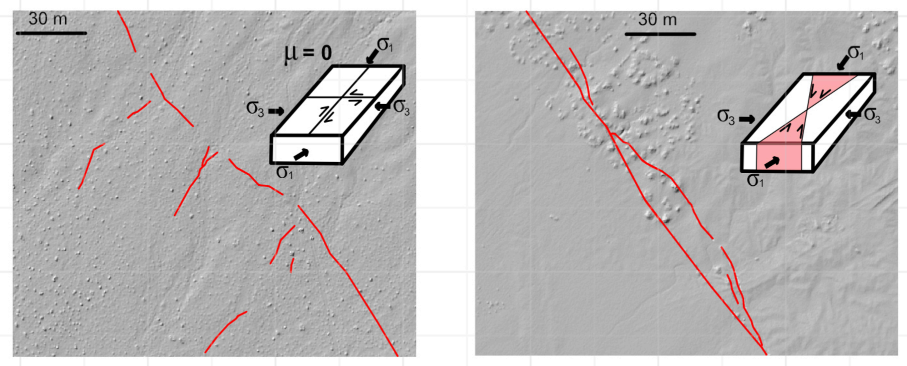

Figure 5: lidar hillshade examples of orthogonal and conjugate fracture sets throughout the rupture.

Slip gradient effects on density

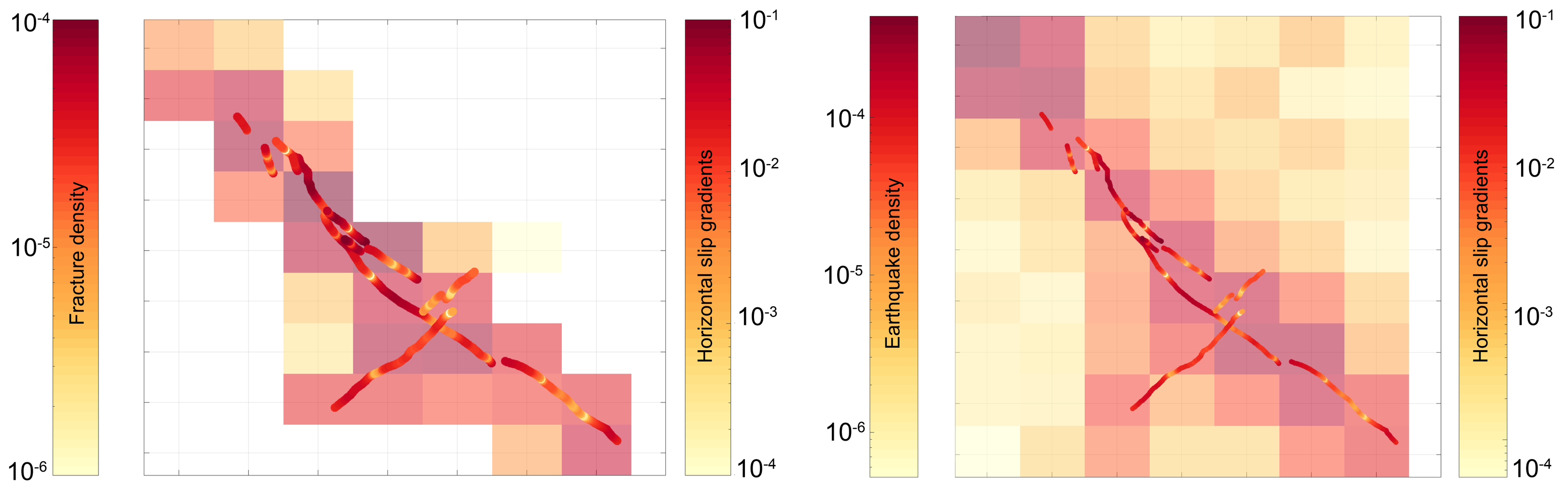

Figure 6: Left: slip gradients (dots) calculated over a 50m window and fracture density (boxes) calculated over a 5km window. Right: slip gradients (dots) and aftershock density (boxes).

We test whether slip gradients drive increases in fracture and aftershock density around the main fault zone. We differentiate on-fault measurements of slip derived from subpixel-correlation of optical imagery (Milliner et al., 2020 - in review), and low-pass filter (50m window) them to remove short-wavelength heterogeneity.

- Fracture density correlates very well with peak gradients for the magnitude 7.1 surface rupture, and overall well for the remainder of the two rupture traces.
- Increased aftershock density still correlates with steep slip gradients but the correlation is a lot weaker than for the fractures. Slip gradient effects may be limited to the very near-surface, influencing only the shallowest aftershocks.

Trends in brittle failure

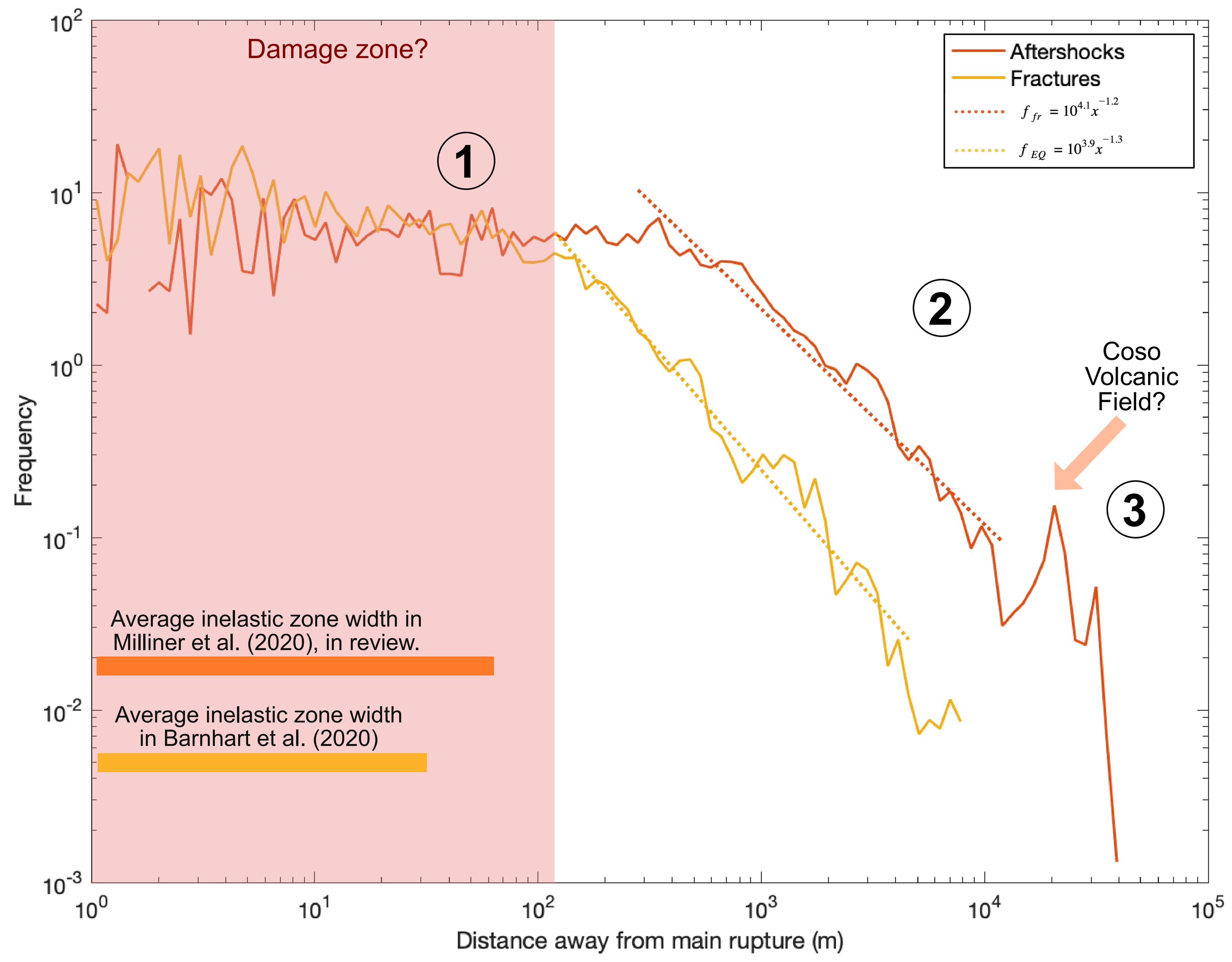

Figure 7: Fracture and aftershock decay with distance away from the fault. The fractures are mapped from 0.5 m near-field and 1m far-field resolution lidar. We limit our analysis to events with relocation errors below 100 m (Ross et al., 2019).

Our analysis illuminates three characteristic regions in the surrounding volume to the main rupture that characterize the decay of brittle deformation with distance away from the fault.

1. A high-stress damage zone where fractures and aftershocks are pervasive within 10^2 meters around the fault characterized by a uniform yield stress.
2. A zone where fracture and aftershock density decay follow comparable inverse power-laws 10^2-10^4 meters away from the fault.

$$f_{fr} = 10^{4.1} x^{-1.2}$$

$$f_{EQ} = 10^{3.9} x^{-1.3}$$

3. An area where fractures cease and aftershocks are influenced by the stress field of the neighboring Coso Volcanic Field.

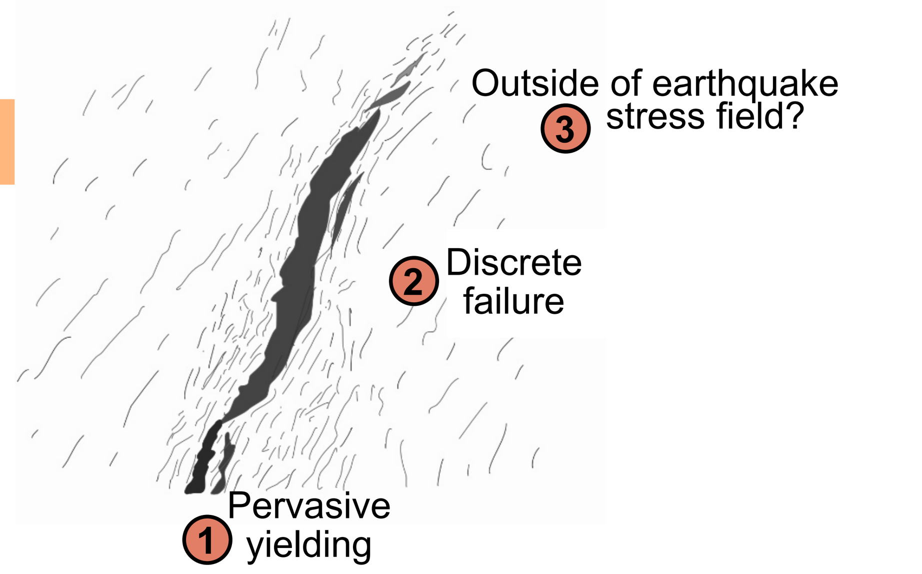

Material properties and aerial strain

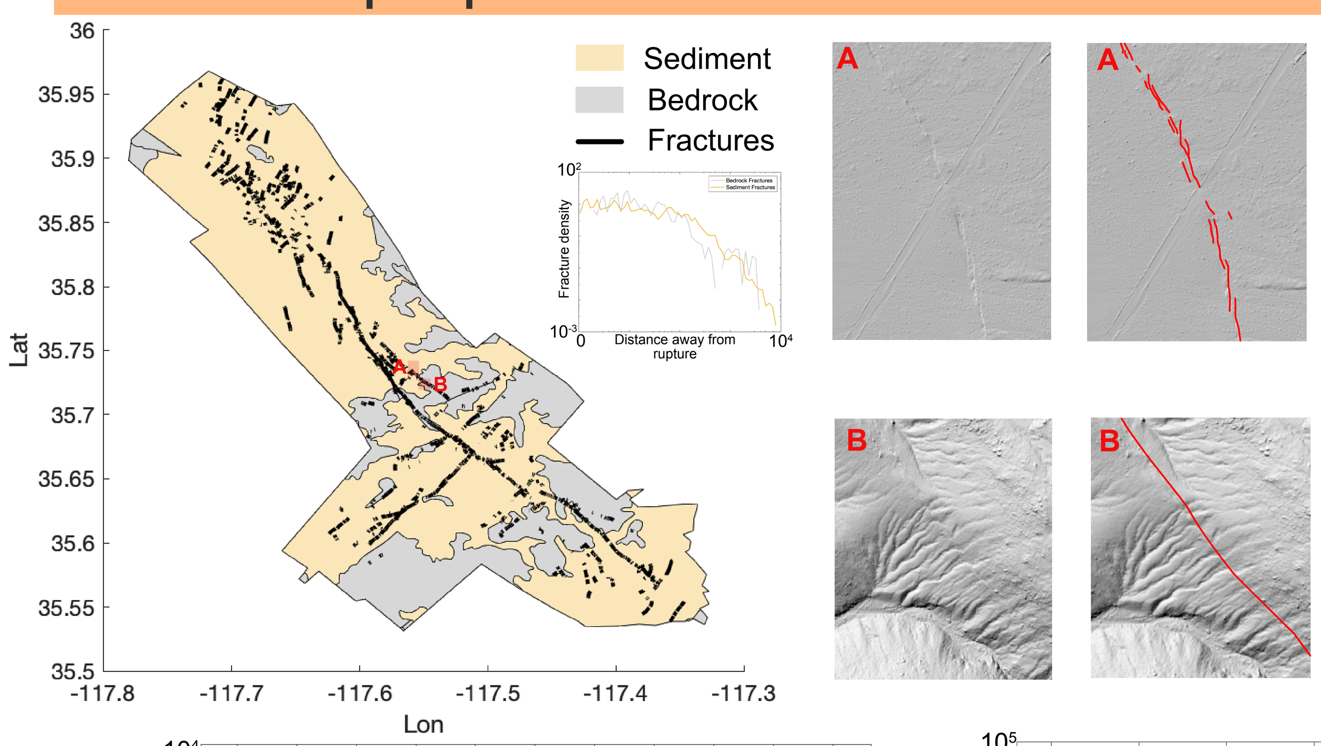

Figure 8: Geologic map of the Ridgecrest area overlaid with the mapped fractures. Inset: bedrock and sediment fracture decay with distance away from the fault. Hillshade insets show the rupture transitioning into lake bed sediment (A) and through bedrock (B). The rupture tends to partition into multiple en-echelon strands when it enters sediment and localizes when breaking through bedrock.

5x10^{-5} fractures/m²

3.5x10^{-6} fractures/m²

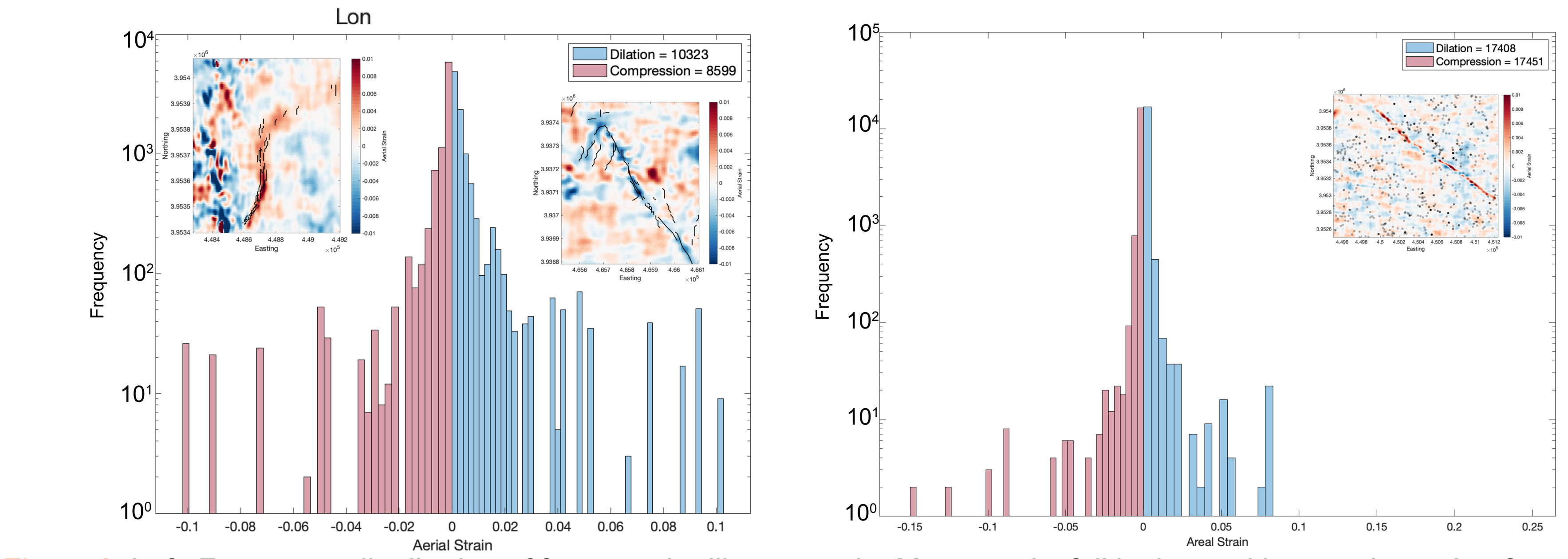

Figure 9: Left: Frequency distribution of fractures in dilatant strain. More cracks fall in the positive quadrants but fracture sets in areas of high positive and negative aerial strain are both present (inset maps from Milliner et al., (2020) in review). Right: Frequency distribution of aftershocks in compressive and dilatant strain. The strain maps get noisier with distance from the fault and the aftershock locations are not precise enough for meaningful comparison.

Discussion

- The presence of conjugate fracture sets in the far-field indicates pre-existing stresses may determine the failure orientation even if failure is dynamically triggered.
- Our fault zone measurements do not rely in assumptions of yield-stress and provide an independent constraint comparable to the inelastic zone widths in geodetic studies (Milliner et al., 2020 submitted; Barnhart et al., 2020).
- Discrete inelastic deformation extends far beyond the damage zone and may build-up to measurable amounts of permanent deformation over several earthquake cycles.

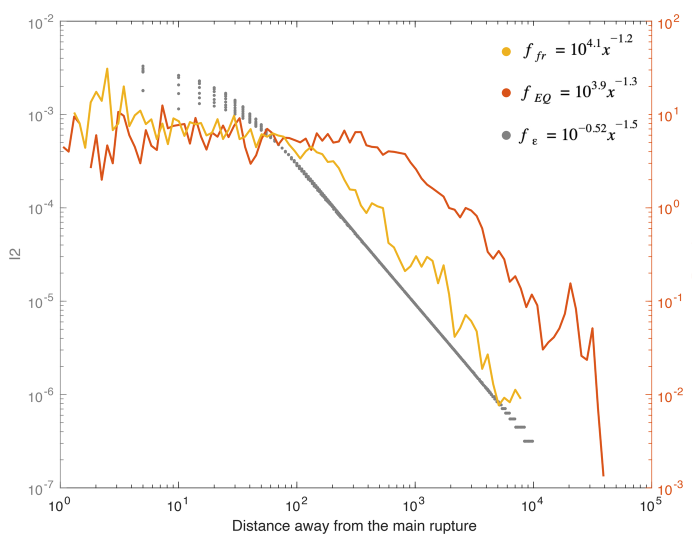

Figure 11: Left Y axis: Elastic prediction for the decay of the second strain invariant with distance away from a dislocation. Right Y axis: Decay of fracture and aftershock density (see figure 7).

- ! Reproducibility test

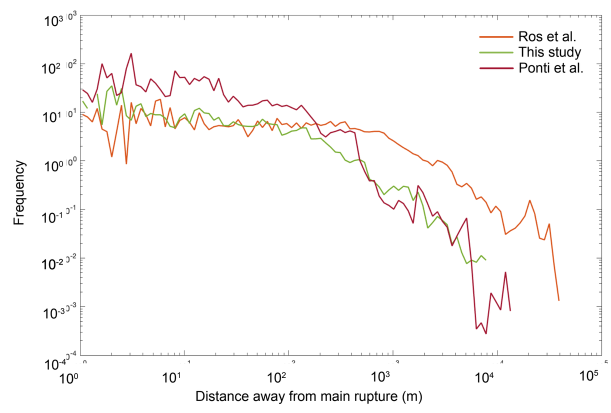

Figure 12: Fracture mapping is subject to decision-making by the mapper, dataset resolution,... Conducting the same analysis as in figure 7 with the fracture map from Ponti et al. (2020), developed combining field data and optical imagery, yields similar results (red) to our fracture map analysis (green).

Acknowledgments

This work was funded through SCEC awards 19209 and 20155 and is SCEC contribution #10578.

Data sources

- EQ catalog - Ross et al., 2019 (Science)
- FMS catalog - Lin, 2020 (SRL)
- On-fault slip and strain maps - Milliner et al. 2020 (in review)
- Displacement maps - Fielding et al. 2020 (SRL)

Connect

@_absrp